crystals

MDPI

Article

Three-Dimensional Flower-like Fe, C-Doped-MoS_2/Ni_3S_2 Heterostructures Spheres for Accelerating Electrocatalytic Oxygen and Hydrogen Evolution

Xuefeng Lv, Guangsheng Liu, Song Liu, Wenting Chen, Dehua Cao, Taize Song, Nannan Wang * and Yanqiu Zhu

Guangxi Institute Fullerene Technology (GIFT), Key Laboratory of New Processing Technology for Nonferrous Metals and Materials, Ministry of Education, School of Resources, Environment and Materials, Guangxi University, Nanning 530004, China; 1815391020@st.gxu.edu.cn (X.L.); 1815301023@st.gxu.edu.cn (G.L.); 1915391010@st.gxu.edu.cn (S.L.); chenwt@st.gxu.edu.cn (W.C.); 1915391230@st.gxu.edu.cn (D.C.); songtaize@sina.com (T.S.); y.zhu@gxu.edu.cn (Y.Z.)

* Correspondence: wangnannan@gxu.edu.cn

Abstract: The exploration of high-efficiency bifunctional electrocatalysts for hydrogen evolution reaction (HER) and oxygen evolution reaction (OER) has long been challenging. The rational design of a catalyst by constructing heterostructures and a doping element are possibly expected to achieve it. Herein, the utilization of flower-like Fe/C-doped-MoS_2/Ni_3S_2-450 spherical structural materials for electrocatalytic HER and OER is introduced in this study. The carboxyferrocene-incorporated molybdenum sulfide/nickel sulfide (Mo_yS_x/NiS) nanostructures were prepared by solvothermal method. After annealing, the iron and carbon elements derived from ferrocenecarboxylic acid enhanced the electrical transport performance and provided rich electronic sites for HER and OER in alkaline media. Specifically, the optimized flower-like Fe/C-doped-MoS_2/Ni_3S_2-450 exhibited efficient bifunctional performance in alkaline electrolyte, with low overpotentials of 188 and 270 mV required to deliver a current density of 10 mA cm^{-2} for HER and OER, respectively. This work provides valuable insights for the rational design of energy storage and conversion materials by the incorporation of transition metal and carbon elements into metal sulfide structures utilizing metallocene.

Keywords: nanosheets; MoS_2/Ni_3S_2; Fe, C-doping; electrocatalysis; hydrogen evolution reaction; oxygen evolution reaction

Citation: Lv, X.; Liu, G.; Liu, S.; Chen, W.; Cao, D.; Song, T.; Wang, N.; Zhu, Y. Three-Dimensional Flower-like Fe, C-doped-MoS_2/Ni_3S_2 Heterostructures Spheres for Accelerating Electrocatalytic Oxygen and Hydrogen Evolution. *Crystals* **2021**, *11*, 340. https://doi.org/10.3390/cryst11040340

Academic Editor: Nguyen Tuan Hung

Received: 18 March 2021
Accepted: 25 March 2021
Published: 28 March 2021

1. Introduction

Environmental problems, such as air pollution and global warming caused by the overuse of fossil fuel, have long been concerning [1–3]. To tackle these environmental problems, attention has been shifted from traditional fuels to efficient and clean energies. H_2 is considered as an ideal clean energy and electrolysis of water to produce hydrogen is a very feasible strategy [4]. The electrochemical overall water splitting process is constituted by the hydrogen evolution reaction (HER) on the cathode side and the oxygen evolution reaction (OER) on the anode side and requires catalysts of outstanding performance promoting the reaction process [5]. Noble metals with promising catalytic properties, such as Pt, RuO_2, and IrO_2, have recently been considered as ideal catalytic materials for HER and OER; both of them correspondingly are used in the anode and cathode reaction as a feasible strategy for overall water splitting [6–8]. However, the utilization of these materials in the electrochemical overall water splitting field is always restricted due to the high cost and rarity [8,9]. With the development of functional materials in nanoscale, significant advances have been made in the study of electrocatalysts, but most electrocatalysts exhibit highly efficient catalytic activity only for HER or OER reactions [4,5,10]. Hence, it is significant to design a low-cost bifunctional catalyst with excellent performance in both HER and OER process to achieve high efficiency overall water splitting.

Most bifunctional catalysts were designed by integrating excellent active components of HER and OER [4]. The as-designed catalysts could efficiently urge active sites to favorably bind towards both oxygen-containing and hydrogen intermediates, reducing the kinetic energy barriers [5]. Molybdenum disulfide (MoS_2), a representative HER catalyst, has widely attracted attention from researchers [11–13] since its free energy of adsorbed H^+ is close to Pt [14,15]. However, MoS_2 is not suitable as a catalyst for OER process because of providing intrinsically poor OER activity [5,16]. It is a feasible strategy to introduce OER active components into MoS_2-based materials to prepare bifunctional catalysts [11,17]. Additionally, nickel sulfides [18–20] exhibited excellent catalytic performance in the OER process due to their unique physicochemical properties. Bolin Li et al. [21] fabricated in situ N-doped Ni_3S_2 nanowires on Ni-foam by high-temperature pyrolysis, which showed excellent performance in OER process, requiring only 271 mV overpotential to achieve a current density of 10 mA/cm^2. Highly durable OER performance was demonstrated by 40 h chronopotentiometry and 10,000 cyclic voltammetry (CV) cycle tests. The rational construction of MoS_2/Ni_3S_2 heterostructures has the potential to achieve highly efficient bifunctional electrocatalysts [22,23]. Furthermore, constructing rational heterostructures could be beneficial to fulfill the synergy in heterostructures, exposing more active sites, promoting catalyst performance, and the electronic transfer. In addition, OER activity of catalysts also could be effectively enhanced by properly doping iron [24,25]. However, their applications also are hampered due to intrinsically low electrical conductivity [4,26]. To prepare a highly conductive catalyst, for a powder catalyst, this is usually achieved by building heterostructures with superior conductive materials, including carbon nanotubes and graphene [27]. C elements derived from metal-organic frameworks (MOFs) also could improve conductivity of electrocatalysts, provide the efficient pathways for charge transport, reduce resistance to charge transfer, and downgrade overpotential of reactions [28–30].

Recently, methods using ferrocene and ferrocenecarboxylic acid to modify electrocatalysts have attracted considerable attention, such as Ziqian Xue et al. [31], who prepared missing-linker metal-organic (MOF) frameworks through modifying Co-BDC with ferrocenecarboxylic acid (Fc), and thus achieved excellent OER performance with ultralow overpotential and current density of 241 mV at 100 mA cm^{-2}, respectively. Pitchai Thangasamy et al. [32] synthesized ferrocene-incorporated cobalt sulfide nanoarchitecture, investigated OER performance, and finally gained rather good results: a Tafel slope of 54.2 mV dec^{-1} and an overpotential as low as 304 mV to drive a current density of 10 mA/cm^2. The authors attribute the enhancing performance of OER to the strong synergistic effect of Fe-based compounds derived from ferrocene. Few studies, however, have been reported for lowering overpotential of HER process by using ferrocenecarboxylic acid. Given all this, considering the different roles of Fe and C elements in catalysts, we decided to prepare an efficient bifunctional catalyst by using the strategy of doped Fc.

Herein, we successfully prepared the flower-like Fe/C-doped-MoS_2/Ni_3S_2-450 (Fe, C-MoS_2/Ni_3S_2-450) sphere structures by doping ferrocenecarboxylic acid and demonstrated the significance of ferrocenecarboxylic acid in the MoS_2/Ni_3S_2 heterostructures on the electrochemical HER and OER. High-resolution transmission electron microscopy (TEM) and X-ray photoelectron spectroscopy (XPS) analysis were carried out to further characterize the structure and surface states of flower-like sphere structures. In our study, the Fe, C-MoS_2/Ni_3S_2-450 represents a low overpotential of 188 mV and 270 mV to drive a current density of 10 mA cm^{-2} for HER and OER, respectively. In this work, we pioneered the use of ferrocenecarboxylic acid-derived iron-carbon doped metal sulfides to enhance the electrical transport performance and increase electronic site for catalytic reaction. This work provides valuable insights for the rational design of energy storage and conversion materials by incorporation of transition metal and carbon elements into metal sulfide structures utilizing metallocene.

2. Results and Discussion

The synthetic procedure of Fe, C-MoS_2/Ni_3S_2-450 is as follows. First, the α-Ni $(OH)_2$ nanosheets were prepared on the basis of previous reports [26]. As shown in Figure S1(see Supporting Information), it can be seen that the formation of well-crystallized α-Ni $(OH)_2$ was corroborated successfully by X-ray diffraction (XRD) pattern (see Figure S1) [33]. The as-prepared $Ni(OH)_2$ product represents nanosheets with smooth surfaces, as shown in the scanning electron microscopy (SEM) image (see Figure S2). The obtained α-Ni $(OH)_2$ was then mixed with sodium molybdate dihydrate, Ferrocenecarboxylic acid (Fc), and thiourea in a suitable proportion through ultrasonic treatment and magnetic stirring. The solution was then transferred into a 100 mL Teflon-lined autoclave reactor and heated to 200 °C for 24 h. After reaction, the as-cooled products were washed several times and collected. To obtain final Fe, C-MoS_2/Ni_3S_2-450, products were annealed at 450 °C in Ar/H_2 (90/10%) environment for 2 h, while the control group was prepared by adjusting the annealing temperatures (400, 450, 500, and 550 °C).

The existence of NiS phase can be confirmed by the XRD pattern shown in Figure 1, in which the diffraction peaks at 2Theta = 18.4°, 32.2°, 35.6°, 40.4°, 48.8°, 50.1°, 52.6°, and 56.25° corresponding to NiS can be clearly observed. By comparison with Joint Committee on Powder Diffraction Standards ((JCPDS) card (No. 12-0041 NiS) [34], it can be seen that the diffraction angles and different crystal faces of NiS phase are corresponding respectively. However, peaks corresponding to different crystal faces of MoS_2 phase were not detected, suggesting the existence of other Mo compounds. Moreover, it could be likely that the MoS_2 phase was formed before annealing under 450 °C for 2 h in Ar/H_2 (90%/10%) environmental atmosphere. As the results shown in Figure 1, three legible peaks are found at the position of 2Theta = 14.3°, 33.5°, 58.3°, which accordingly correspond to (002), (101), (110) crystal planes of MoS_2 phases (JCPDS no. 37-1492-MoS_2) [35]. In addition, other obvious diffraction peaks appear in 2Theta = 21.8°, 31.1°, 37.8°, 44.2°, 49.8°, 50.1°, 55.2°, corresponding to (101), (110), (003), (202), (113), (211), (122) crystal planes of Ni_3S_2 phases (JCPDS no. 44-1418-Ni_3S_2) [21], respectively, indicating the transformation from NiS phase to Ni_3S_2 phase. This might result from the breaking of partial Ni-S bonds, allowing S- and Mo- sites to combine and form MoS_2 due to the annealing process at 450 °C for 2 h in Ar/H_2 (90%/10%) environmental atmosphere. According to previous work [5], MoS_2 could exhibit excellent catalytic performance in HER process and edge sites of MoS_2 and sulfur anion vacancies could provide sites for increased HER activity. It is shown that annealing temperature is a key factor affecting the hydrogen evolution performance of the catalyst. In order to investigate the elemental surface distribution and valence state of catalyst, Raman measurement was carried out to measure the surface states of flower-like sphere structures. As shown in Figure 1b, the peaks at 298, 370, and 403 cm^{-1} are corresponding to E_{1g}, $E^1{}_{2g}$, and A_{1g} modes of 2H-MoS_2, while the peak at 315 cm^{-1} is from the modes of Ni_3S_2 [4]. The peak located at 345 cm^{-1} belongs to the modes of MoS_2/Ni_3S_2 [22,23]. In addition, three sharp peaks can be observed between 800–1000 cm^{-1}, indicating the molecular structure of Mo_3S_{13} distributing on edge sites of MoS_2 and the existence of rich under-coordinated Mo-S edge sites in the Fe, C-MoS_2/Ni_3S_2-450.

As shown in the SEM figures (Figure 2a), the reaction products of $Ni(OH)_2$, $Na_2MoO_4{\cdot}2H2O$, Fc, and thiourea display three-dimensional flower-like sphere structures. A large number of nanosheets on the sphere surface can be observed, which may result in the increase of effective active sites and promote performances of the catalyst. Moreover, once the feeding rate of $Ni(OH)_2$ was increased, the product evolved from flower-like spherical structures to irregular forms or spheroidal particles distributed on the previous flower-like spherical surface. To maintain the preferable nanosheet structure, an optimal $Ni(OH)_2/Na_2MoO_4$ (the amount of Na_2MoO_4 remained at 2 mmol) feeding ratio of 0.2g/Na_2MoO_4 was adopted for the fabrication. As shown in the SEM images (Figure 2b,c), samples at different magnifications clearly reveal the existence of that original three-dimensional flower-like spherical structure, with ultrathin nanosheets distributed evenly on the surface. This result can be further confirmed by the TEM image shown in Figure 2d–g, in which an irregular sphericity

structure of Fe, C-MoS_2/Ni_3S_2-450, with its interior clearly shaded, can be observed, suggesting the whole structure is not in a hollow state. The TEM images in Figure 2e,f further confirm the formation of flower-like Fe, C-MoS_2/Ni_3S_2-450 spheres. In Figure 2g, the lattice fringe of 0.62 nm belongs to the (002) lattice plane of MoS_2 [22], while the lattice distances of 0.28 nm are indexed to the (110) plane of Ni_3S_2, as the (110) plane of Ni_3S_2 and the neighboring (002) plane of MoS_2 constitute the interface of MoS_2/Ni_3S_2 heterostructures [22]. In conclusion, the flower-like spherical structure of Fe, C-MoS_2/Ni_3S_2-450 synthesized in this work has good uniformity in both structure and size.

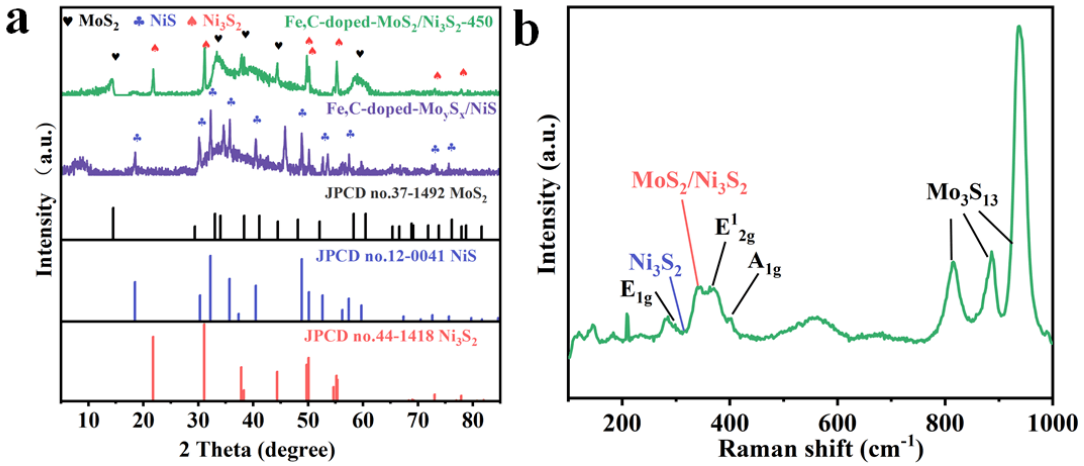

Figure 1. (**a**) XRD patterns of Fe, C-Mo_yS_x/NiS and Fe, C-MoS_2/Ni_3S_2-450, (**b**) Raman spectrum of the Fe, C-MoS_2/Ni_3S_2-450.

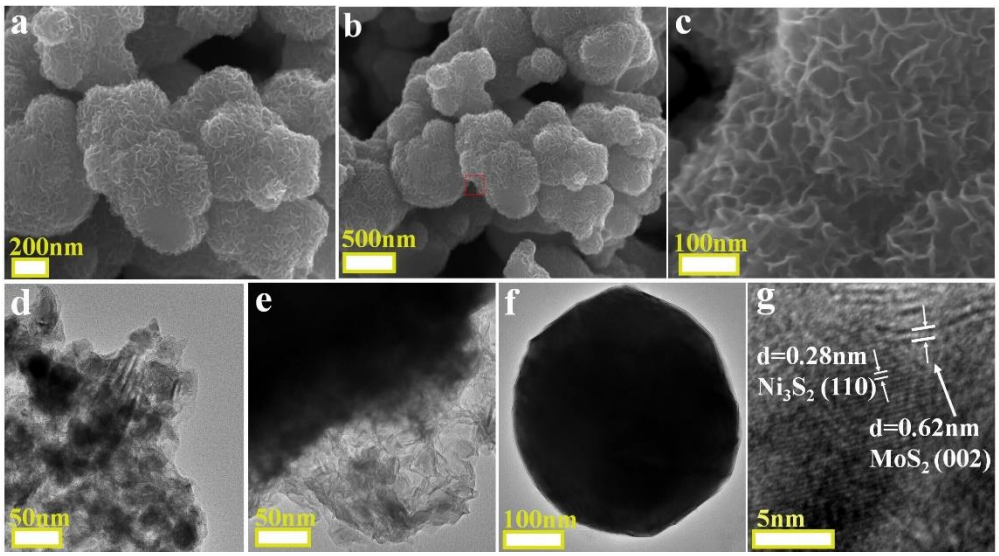

Figure 2. (**a**) SEM image of Fe, C-Mo_yS_x/NiS, (**b**,**c**) Fe, C-MoS_2/Ni_3S_2-450; (**d**–**g**) TEM image of Fe, C-MoS_2/Ni_3S_2-450.

The results of XPS measurement are shown in Figure 3, where in the Ni 2p is composed of the alike characteristic spin-orbit states of Ni $2p_{1/2}$ and Ni $2p_{3/2}$, which are accordingly corresponding to the strong peaks at 857.0 eV and 874.0 eV in the upper half of Figure 3a, with its two weak satellite peaks located at 862.1 eV and 879.5 eV, respectively. Comparing with the lower half of Figure 3a, there were significant positive shifts for peaks of Ni 2p and obvious changes of chemical valence states. After annealing in reducing atmosphere, it is possible that the Fe doping brings identifiable chemical state variation of Ni compared to Fe, C-Mo_yS_x/NiS. The result above is similar to the previous report [22], and can endow catalysts with more active sites for OER process [25]. For the Mo 3d spectrum in Figure 3b, the two peaks at about 229.6 and 232.8 eV are corresponding to Mo^{4+} $3d_{5/2}$ and Mo^{4+} $3d_{3/2}$.

In addition, the peak located at 236.2 eV indicates the presence of a high oxidation state of Mo^{6+}, which might be due to the existing Mo^{6+} that has not been fully reduced before annealing. The chemical valence of Mo has significant change: the peaks belonging to Mo^{6+} decrease noticeably in Fe, C-MoS_2/Ni_3S_2-450 as compared with Fe, C-Mo_yS_x/NiS, illustrating that MoS_2 is generated. The peak at about 226.7 eV originates from S 2s, indicating the existence of the chemical bindings of Mo-S. The S 2p spectrum in Figure 3c deconvolutes into two peaks, which accordingly correspond to S $2p_{1/2}$ (163.5 eV) and S $2p_{3/2}$ (162.4 eV), suggesting the existence Mo-S and Ni-S. The nearby peak located at 168.9 eV belongs to the satellite peak of S 2p.

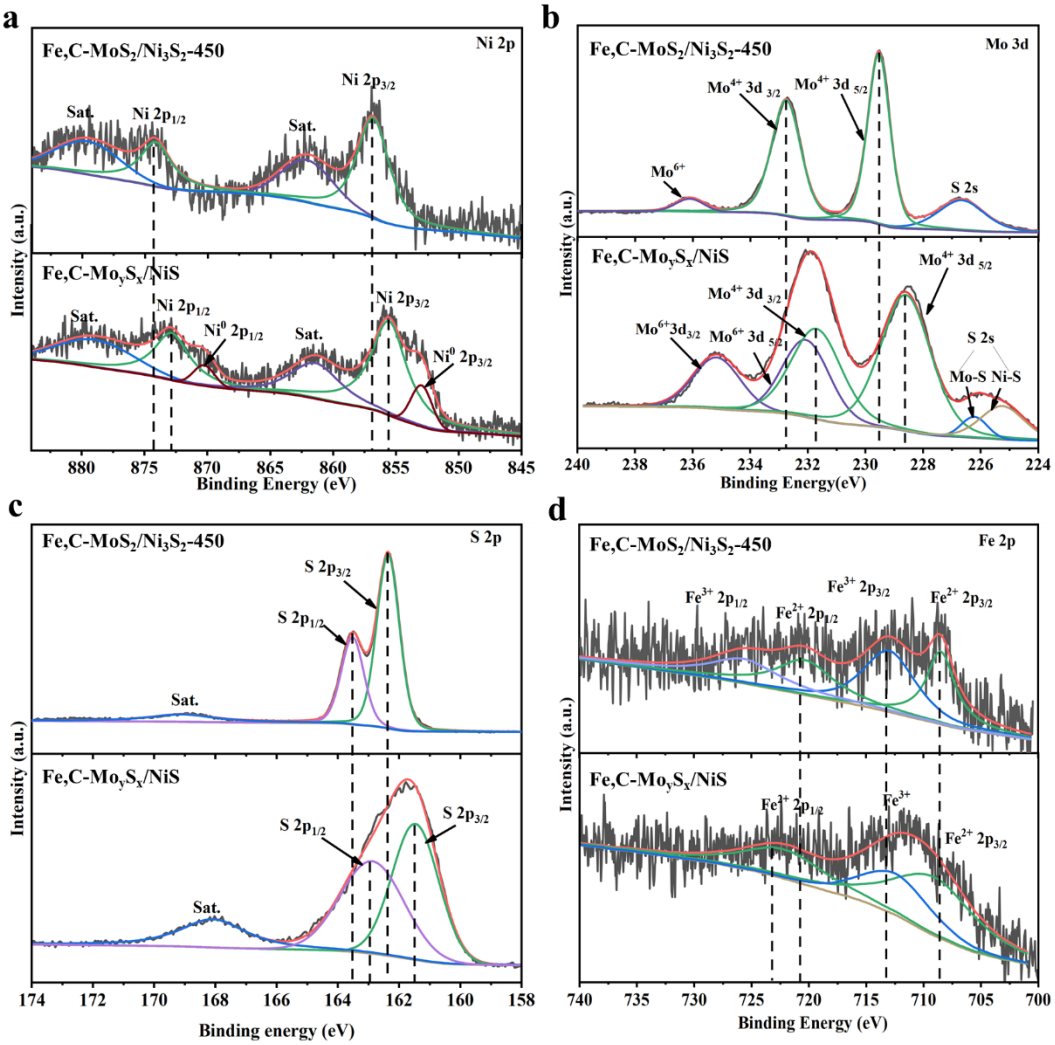

Figure 3. XPS spectra of Fe, C-MoS_2/Ni_3S_2-450 and Fe, C-Mo_yS_x/NiS: high-resolution XPS analysis of (**a**) Ni 2p, (**b**) Mo 3d, (**c**) S 2p, (**d**) Fe 2p spectra.

As shown in Figure 3c, the peak of S $2p_{1/2}$ is belonging to the sulfur with low coordination and has a relationship with sulfur defects, which indicates the possibility of abundant defects in Fe, C-MoS_2/Ni_3S_2-450. It may be significant for HER performances. In Figure 3d, the Fe 2p peaks of Fe, C-MoS_2/Ni_3S_2-450 can be deconvoluted, four peaks at 708.3 eV (Fe^{2+} 2p3/2) and 720.5 eV (Fe^{2+}2p1/2), 713.5 eV (Fe^{3+}2p3/2) and 726.0eV (Fe^{3+}2p1/2), suggesting the Fe^{2+} compounds and Fe^{3+} compounds. However, comparing with the Fe 2p spectrum in the lower half of Figure 3d, we clearly find that the binding energy of Fe 2p got shifted further to the left and the amount of Fe^{2+} species was decreased, suggesting partial original Fe^{2+} transformation into Fe^{3+}. To investigate the effect of temperature on chemical shifts of Ni, Mo, S, and Fe, XPS measurements were performed on Fe, C-Mo_yS_x/NiS

(Figure 3a–d) for comparison. It can be seen that large shifts of binding energy of Ni and Mo, S, Fe, and the heterostructure relationship of MoS_2 and Ni_3S_2 could be strengthened after annealing [4,22]. In addition, annealing changes the chemical environment of Fe, C-MoS_2/Ni_3S_2-450 and treatment chemical state of Fe and Ni elements and may affect catalytic activity.

The electrocatalytic HER and OER performance of the Fe, C-MoS_2/Ni_3S_2-450 flower-like spherical structures were measured in a three-electrode configuration and alkaline electrolyte (1M KOH, PH = 14). Meanwhile, the performance of the commercial Pt/C, RuO_2, and MoS_2, NiS_2, MoS_2/Ni_3S_2 were also investigated. Figure 4a illustrates the polarization curves of the samples obtained at a scan rate of 5 mV/s (corrected with IR compensation already, unless otherwise noted). It can be seen that Fe, C-MoS_2/Ni_3S_2-450 exhibits superior HER activity compared to those of MoS_2, NiS_2, and MoS_2/Ni_3S_2 as the potential increasing. To achieve a current density of 10 mA/cm^2, a low overpotential of 188 mV should be affordable for Fe, C-MoS_2/Ni_3S_2-450. However, upon comparison among MoS_2/Ni_3S_2 (315mV), NiS_2 (334 mV), and MoS_2 (363 mV), the advantages of Fe and C for effectively promoting the HER activity of MoS_2/Ni_3S_2 could be found. In addition, samples obtained in different annealing temperatures in atmospheres of Ar/H_2 (90%/10%) were also prepared for comparison. As shown in Figure 4f, the HER performance of the Fe, C-MoS_2/Ni_3S_2-450 were effectively improved when temperature was increased, and reached optimum effect at the temperature of 450 °C. However, the catalytic reaction process of Fe, C-MoS_2/Ni_3S_2-450 became worse when the annealing temperature exceeded 450 °C. According to XRD analysis (Figure 1a), it is possible that Ni_3S_2 and MoS_2 phase were formed, and thus the electrocatalytic performance of catalysts were modified. It is a practicable method to enhance catalytic properties in some materials' systems through doping catalytic materials with transition-metal atoms. Meanwhile, according to previous reports [25], the catalytic performance of electrocatalysts could be increased, through adjusting their coordination valence states and chemical environment by doping a small amount of Fe. Therefore, the Fe, C-MoS_2/Ni_3S_2-450 in this study exhibited much higher HER performance than that of MoS_2/Ni_3S_2, which might result from the introduction of Fe and C elements.

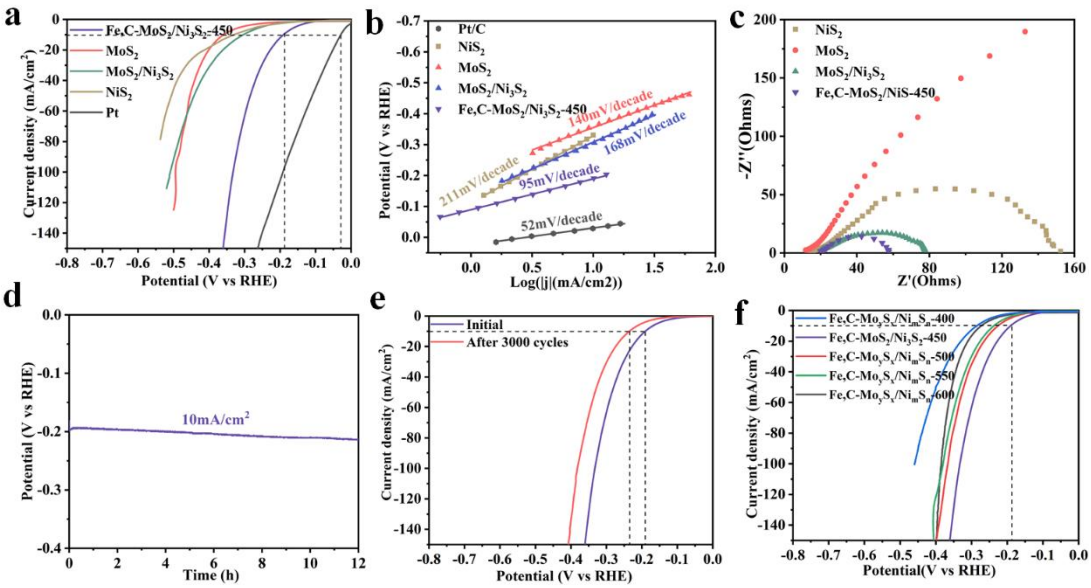

Figure 4. (**a**) Polarization curves and (**b**) the corresponding Tafel plots; (**c**) electrochemical impedance spectroscopy (EIS) analysis of the obtained sample for hydrogen evolution reaction (HER). (**d**) Chronopotentiometric curve of HER for the Fe, C-MoS_2/Ni_3S_2-450. (**e**) Linear sweep voltammetry LSV polarization curves of the Fe, C-MoS_2/Ni_3S_2-450 before and after 2000 cycles. (**f**) LSV polarization curves of samples by different annealing temperatures.

To further investigate the HER activity, the Tafel plots from polarization curves were fitted. As shown in Figure 4b, the Tafel slope of the Fe, C-MoS_2/Ni_3S_2-450 (95 mV/decade) is lower than that of pure MoS_2/Ni_3S_2 (168 mV/decade), MoS_2 (140 mV/decade), and NiS_2 (211 mV/decade), indicating that Fe, C-MoS_2/Ni_3S_2-450 has faster reaction kinetics. According to previous reports [4,22], three principal steps are involved in HER, with different Tafel slopes corresponding to associated reaction steps. The first step is Volmer reaction (a Tafel slope of about 120 mV/decade), the second step is Heyrovsky reaction (a Tafel slope of about 40 mV/decade) or Tafel reaction (a Tafel slope of about 30 mV/decade). According to the Tafel slope of Fe, C-MoS_2/Ni_3S_2-450 (−95 mV/decade), its HER could follow the Volmer−Heyrovsky mechanism ($H_2O + H_{ads} + e^- \rightarrow H_2 + OH^-$), where H_{ads} represents the H atom on an active site. Meanwhile, the smaller Tafel slopes stand for faster electrocatalytic kinetics of HER and OER.

In addition, electrochemical impedance spectroscopy (EIS) analysis at −0.25 V (V vs. reversible hydrogen electrode (RHE)) was carried out for the in-depth study of the activity of electrocatalytic kinetics of HER. As shown in Figure 4c, it can be seen that charge-transfer resistance in MoS_2, NiS_2, MoS_2/Ni_3S_2, and Fe, C-MoS_2/Ni_3S_2-450 was illustrated by Nyquist. Among all the samples, the lowest charge transfer resistance (R_{ct}) occurred in Fe, C-MoS_2/Ni_3S_2-450, suggesting faster electrocatalytic kinetics of HER activities and expediting of the Faradaic process on electrode. Hence, the result further reveals that the charge-transfer process of MoS_2/Ni_3S_2 can be accelerated by doping C element.

Electrochemical stability of the catalysts is taken as standard for judging the HER performance of catalyst. The long-term stability of Fe, C-MoS_2/Ni_3S_2-450 was obtained using chronoamperometry and CV test. As shown in Figure 4d (a constant current density of 10 mA/cm^2 and time of 12 h), potential of the Fe, C-MoS_2/Ni_3S_2-450 was enhanced to only 25 mV over 12 h at 10 mA/cm^2. The Fe, C-MoS_2/Ni_3S_2-450 exhibited superior stability of HER with only 47 mV degradation in potential after 3000 CV cycles (see Figure 4e).

It is known that catalytic performance is positively correlated with electrochemically active surface areas (ECSA), and ECSA also shows a positive correlation with the double-lay capacitance (C_{dl}). It is therefore C_{dl} was obtained from cyclic voltammetry (CV) curves to further evaluate the HER catalytic performance. Based on CV curves (Figure S3), the C_{dl} values of the NiS_2 (0.15 mF/cm^2), MoS_2 (0.24 mF/cm^2), MoS_2/Ni_3S_2 (0.85 mF/cm^2), and Fe, C-MoS_2/Ni_3S_2-450 (1.04 mF/cm^2) were obtained. Through comparison, it can be seen that Fe, C-MoS_2/Ni_3S_2-450 shows the highest C_{dl} value, meaning higher ECSA of as-obtained Fe, C-MoS_2/Ni_3S_2-450 because of the Fe and C incorporation. The result reveals that the Fe and C incorporation effectively provide more electroactive catalytic sites that lead to enhanced HER performance.

Since electrochemical water splitting is composed of HER and OER processes, it is very necessary to further investigate the OER performance of Fe, C-MoS_2/Ni_3S_2-450. In the polarization curves of OER (see Figure 5a), the lowest overpotential of 273 mV at a current density of 10 mA/cm^2 is observed in Fe, C-MoS_2/Ni_3S_2-450 (350 mV for RuO_2, 400 mV for NiS_2, 460 mV for MoS_2, and 355 mV for MoS_2/Ni_3S_2), suggesting the superior OER performance of flower-like MoS_2/Ni_3S_2 spheres were improved by doping Fe and C. According to previous reports [25], Fe element has a unique catalytic ability in OER, and suitable doping of Fe helps the low valence state of Ni^0 in metal oxide/(oxy)hydroxide materials to shift to more active $Ni2^+$ with a high valence state in OER activity and optimize the absorption energies of O and OH binding, causing the OER performance to improve.

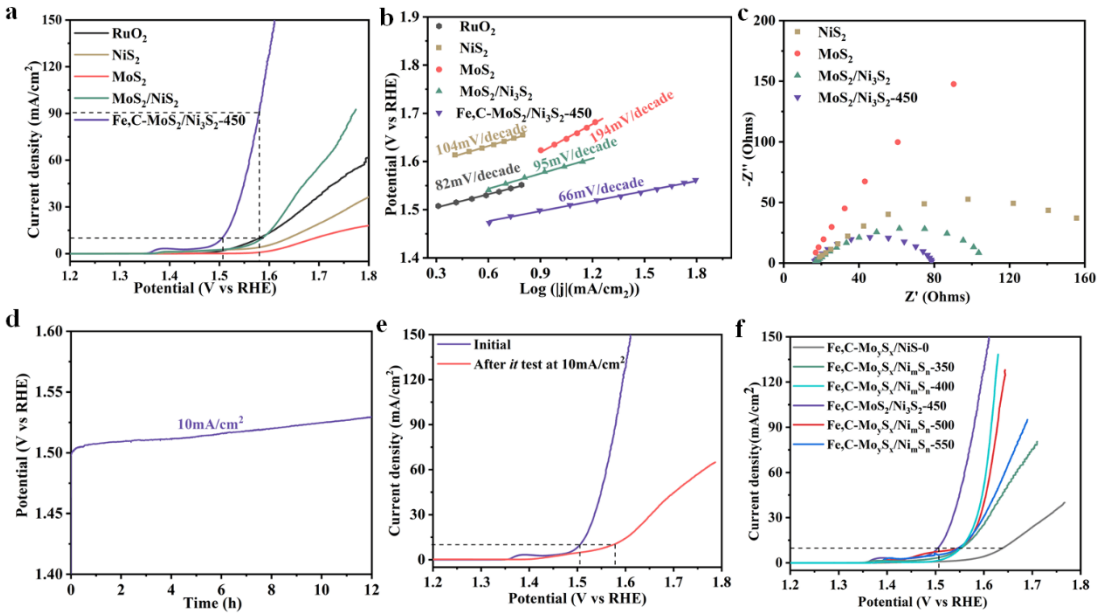

Figure 5. (**a**) Polarization curves and (**b**) the corresponding Tafel plots. (**c**) EIS analysis of the obtained sample for OER. (**d**) Chronopotentiometric curve of HER for the Fe, C-MoS_2/Ni_3S_2-450 (**e**) LSV polarization curves of the Fe, C-MoS_2/Ni_3S_2-450 before and after *i-t* test (The stability test was carried out by the *i-t* curve) at 10 mA/cm^2. (**f**) LSV polarization curves of samples by different annealing temperatures.

Likewise, the Tafel plots from polarization curves were fitted to further investigate OER activities. As shown in Figure 5b, a Tafel slope of only 66 mV/decade was observed in Fe, C-MoS_2/Ni_3S_2-450, which is superior to the RuO_2 (82 mA/decade), the NiS_2 (104 mA/decade), the MoS_2 (194 mA/decade), and MoS_2/Ni_3S_2 (95 mA/decade). This result reveals the enhanced reaction kinetic of Fe, C-MoS_2/Ni_3S_2-450.

In addition, EIS (at 1.48 V (vs. RHE), Figure 5c) and chronoamperometry (a constant current density of 10 mA/cm^2 and time of 12 h, Figure 5d) tests were carried out to investigate the OER performance of the Fe, C-MoS_2/Ni_3S_2-450. As with the HER activity, the lowest R_{ct} in Fe, C-MoS_2/Ni_3S_2-450 indicates the faster Faradaic process on the Fe, C-MoS_2/Ni_3S_2-450 heterostructures, resulting in excellent OER performance Fe, C-MoS_2/Ni_3S_2-450. As shown in Figure 4d, the Fe, C-MoS_2/Ni_3S_2-450 maintains a high stability at 10 mA/cm^2, but the left-hand of the chronoamperometry curve has an upward trend. The increased contact resistance between the catalyst and the electrolyte was due to the bubbles from the OER reaction that could not overflow instantly. However, the bubbles busted and disappeared as they became overgrown. After *it* test (The stability test was carried out by the *i-t* curve) at 10 mA/cm^2, the overpotential of the Fe, C-MoS_2/Ni_3S_2-450 reached 60 mV in Figure 5e. To find the best annealing temperature, different samples were prepared to test OER activity by changing the annealing temperature. The result shown in Figure 5f reveals that the lowest overpotential of OER at 10 mA/cm^2 occurred in samples annealed at 450 °C, and thus indicate the best OER performance.

In conclusion, the improved HER and OER performance of the Fe, C-MoS_2/Ni_3S_2-450 originated from the doping C element, which resulted in better electrical transport performance with lower overpotential and rich electronic sites for catalytic reaction after suitable annealing. In addition, the doping of Fe helped to enhance the interfacial effects between MoS_2 and Ni_3S_2, as the Fe caused the low valence state of coordinated metals to shift to a more active high valence, optimized the heterostructure, and enhanced the reaction kinetics of OER.

3. Conclusions

In summary, 3-dimensional flower-like Fe, C-doped MoS_2/Ni_3S_2 heterostructural spheres were successfully synthesized via a hydrothermal reaction with Fc (ferrocenecar-

boxylic acid) followed by annealing. After annealing, two phases of MoS_2 and Ni_3S_2 phase originating from Mo_yS_x/NiS phase were formed, as further confirmed by XRD patterns. The flower-like Fe, C-doped MoS_2/Ni_3S_2 exhibits high HER and OER performance in alkaline-solution environment, wherein the OER is even superior to those of commercial RuO_2. Long-time stability was also exhibited, along with a low overpotential of 273 mV at a current density of 10 mA/cm^2 and a Tafel slope as low as 66 mV/decade. Comparing with doping ferrocenecarboxylic acid or ferrocene, our Fe, C-doped catalyst presents a superior HER performance with a very small overpotential of 188 mV at 10 mA/cm^2. The strong synergistic effect of Fe and C elements derived from Fc with MoS_2/Ni_3S_2 further enhances the transfer of electrons and thus provides a rich active site for catalytic reaction.

4. Experimental Section

4.1. Reagents and Chemicals

Nickel chloride hexahydrate ($NiCl_2 \cdot 6H_2O$), hexamethylenetetramine (HMT), sodium molybdate dihydrate ($Na_2MoO_4 \cdot 2H_2O$), ferrocenecarboxylic acid (Fc), thiourea, potassium hydroxide (KOH), and commercial 20 wt.% Pt/C and RuO_2 were purchased from Lan Tian Commodities Co. Ltd (Nanning, China). All the reagents were used directly without further purification. The Milli-Q water (18.2 MΩ, Millipore) was in all experiments.

4.2. Preparation of Ni(OH)$_2$ Precursor

The method of preparing $Ni(OH)_2$ precursor referred to previous work and modified it [26]. An amount of 3 mmol of $NiCl_2 \cdot 6H_2O$ and 5g HMT were added to a beaker of 100 milliliters of Milli-Q water, stirred to obtain a green homogeneous solution. Then, the green solution was heated at 90 °C for 4 h. The green products were washed by centrifugation with Milli-Q water, dried at 70 °C in air, and collected.

4.3. Preparation of Fe, C-Mo$_y$S$_x$/NiS and Mo$_y$S$_x$/NiS

An amount of 0.2 g of pre-fabricated $Ni(OH)_2$ precursor was dissolved in 20 ml of Milli-Q water with stirring for 5 min. Then, 2 mmol of $Na_2MoO_4 \cdot 2H_2O$ and 12 mmol of thiourea were added to the previous solution under continuous magnetic stirring for some time. In the meantime, 40 ml of glycol was instilled. After obtaining a homogeneous solution, 0.1 mmol of Fc continued to be added. The solution was treated with ultrasound for 30 min at room temperature and transferred to a 100 mL Teflon-lined autoclave reactor with heating to 200 °C for 24 h. After the reaction, the obtained were washed by centrifugation with ethanol, dried at 60 °C in air, and collected. The obtained samples were sighted as Fe, C-Mo_yS_x/Ni_yS_x. To prepare the Mo_yS_x/Ni_yS_x, the step of adding 0.1 mmol of Fc was omitted; other steps had no change.

4.4. Preparation of Fe, C-MoS$_2$/Ni$_3$S$_2$ or MoS$_2$/Ni$_3$S$_2$

An amount of 0.1 g of the Fe, C-MoS_2/Ni_3S_2 or the MoS_2/Ni_3S_2 was put in the porcelain boat. Then, the sample was heated to 450 °C with a rate of 2 °C/min for 120 min under Ar/H_2 (90%/10%) atmosphere.

4.5. Preparation of MoS$_2$

The amounts of 1 mmol of $Na_2MoO_4 \cdot 2H_2O$ and 6 mmol of thiourea were added to 60 ml of Milli-Q water, with stirring for 15 min, and transferred to a 100 mL Teflon-lined autoclave reactor with heating to 200 °C for 24 h. After the reaction, the obtained were washed by centrifugation with ethanol, dried at 60 °C in air, and collected.

4.6. Preparation of NiS$_2$

An amount of 0.1 g of pre-fabricated $Ni(OH)_2$ precursor was put in the porcelain boat; 0.2 g of sublimed sulfur was put upstream of the porcelain boat. Then, the furnace was heated to 400 °C with a rate of 2 °C/min for 120 min under N_2 atmosphere.

5. Materials Characterization

To ascertain the structures and morphologies, the prepared samples were tested by XRD (Rigaku D/max 2500 V) with a Cu Kα radiation (λ = 0.15406 nm, 40 kV, 40 mA), SEM (Sigma 300, operating at 10 kV), TEM (FEI TEGNAI G2 F30, operating at 200 kV). Raman (Thermo Fischer DXR, λ = 532 nm) and XPS (ESCALAB 250XI) spectra were used to analyze for the surface states.

6. Electrochemical Measurement

All electrochemical performances were measured in a three-electrode system with the electrochemical workstation (CHI660E) at room temperature. During electrochemical measurements of the HER and OER, working electrode (reversible hydrogen electrode (RDE), d = 3 mm, RED MATRIX CHINA LIMITED, 1600 rpm), mercuric oxide electrode (Hg/HgO) as the reference electrode, carbon rod, and Pt foil as the counter electrode for OER and HER, respectively, were used. For the catalyst ink prepared, 5 mg of samples were dispersed in 770 μL of Milli-Q water, 200 μL of ethanol, and 30 μL of Nafion (5 wt.%) via ultrasonication. Then, 5 μL of the catalyst ink was loaded to the surface of the working electrode (a mass of 35 mg/cm^2) to test electrochemical performances after drying. The electrochemical performances were evaluated by linear sweep voltammetry (LSV), cyclic voltammetry (CV), electrochemical impedance spectroscopy (EIS), and chronoamperometry. N_2 and O_2 were inputted continuously to the 1M KOH solution before the HER and OER measurements were evaluated by linear sweep voltammetry LSV (at a scan rate of 5 mV/s), respectively. In order for a comparison with previous work, all the potentials were calibrated to the reversible hydrogen electrode (RHE) via $E_{\text{vs. RHE}} = E_{\text{vs. Hg/HgO}} + 0.059 \times PH + 0.098$.

Supplementary Materials: The following are available online at https://www.mdpi.com/article/10.3390/cryst11040340/s1, Figure S1. XRD patterns of $Ni(OH)_2$; Figure S2. SEM image of $Ni(OH)_2$; Figure S3 exhibits EDX mapping images of the Fe, C-MoS2/Ni3S2-450, indicating the the presence of C, S, Fe, Ni and Mo element; Figure S4 EDX analysis images of the Fe, C-MoS2/Ni3S2-450; Figure S5 (a) XPS survey and (b) C 1s spectrum of the Fe, C-MoS2/Ni3S2-450 and Fe, C-MoySx/NiS; Figure S6. (a–d) CV curves of obtained samples in the window of 0.94-1.04 V vs. RHE. (e) estimated Cdl values.

Author Contributions: Conceptualization, X.L., G.L., and S.L.; writing-original draft preparation, X.L., G.L., D.C., and W.C.; experiment, D.C. and T.S.; funding acquisition, N.W., Y.Z. All authors have read and agreed to the published version of the manuscript.

Funding: This research was funded by the National Nature Science Foundation, grant number 51972068.

Acknowledgments: This work was supported by the grants from the National Natural Science Foundation (grant NO: 51972068) and Guangxi Key Laboratory of Processing for Non-Ferrous Metals and Featured Materials.

Conflicts of Interest: The authors declare no conflict of interest.

References

1. Li, P.; Li, W.; Chen, R.; Lin, Y. Boosting the Oxygen Evolution Electrocatalysis Performance of Iron Phosphide via Architectural Design and Electronic Modulation. *ACS Sustain. Chem. Eng.* **2020**, *8*, 9206–9216. [CrossRef]
2. Luo, Y.; Tang, L.; Khan, U.; Yu, Q.; Cheng, H.M.; Zou, X.; Liu, B. Morphology and surface chemistry engineering toward pH-universal catalysts for hydrogen evolution at high current density. *Nat. Commun.* **2019**, *10*, 269. [CrossRef]
3. Roger, I.; Shipman, M.A.; Symes, M.D. Earth-abundant catalysts for electrochemical and photoelectrochemical water splitting. *Nat. Rev. Chem.* **2017**, *1*, 3. [CrossRef]
4. Lin, J.; Wang, P.; Wang, H.; Li, C.; Si, X.; Qi, J.; Cao, J.; Zhong, Z.; Fei, W.; Feng, J. Defect-Rich Heterogeneous MoS2/NiS2 Nanosheets Electrocatalysts for Efficient Overall Water Splitting. *Adv. Sci.* **2019**, *6*, 1900246. [CrossRef] [PubMed]
5. Bao, J.; Zhou, Y.; Zhang, Y.; Sheng, X.; Wang, Y.; Liang, S.; Guo, C.; Yang, W.; Zhuang, T.; Hu, Y. Engineering water splitting sites in three-dimensional flower-like Co–Ni–P/MoS2 heterostructural hybrid spheres for accelerating electrocatalytic oxygen and hydrogen evolution. *J. Mater. Chem. A* **2020**, *8*, 22181–22190. [CrossRef]

6. Deng, X.; Kang, X.; Li, M.; Xiang, K.; Wang, C.; Guo, Z.; Zhang, J.; Fu, X.-Z.; Luo, J.-L. Coupling efficient biomass upgrading with H2 production via bifunctional CuxS@NiCo-LDH core–shell nanoarray electrocatalysts. *J. Mater. Chem. A* **2019**, *8*, 1138–1146. [CrossRef]
7. Zhong, C.; Han, Z.; Wang, T.; Wang, Q.; Shen, Z.; Zhou, Q.; Wang, J.; Zhang, S.; Jin, X.; Li, S.; et al. Aliovalent fluorine doping and anodization-induced amorphization enable bifunctional catalysts for efficient water splitting. *J. Mater. Chem. A* **2020**, *8*, 10831–10838. [CrossRef]
8. Yu, F.; Zhou, H.; Huang, Y.; Sun, J.; Qin, F.; Bao, J.; Goddard, W.A., 3rd; Chen, S.; Ren, Z. High-performance bifunctional porous non-noble metal phosphide catalyst for overall water splitting. *Nat. Commun.* **2018**, *9*, 2551. [CrossRef]
9. Shi, H.; Zhou, Y.-T.; Yao, R.-Q.; Wan, W.-B.; Ge, X.; Zhang, W.; Wen, Z.; Lang, X.-Y.; Zheng, W.-T.; Jiang, Q. Spontaneously separated intermetallic Co3Mo from nanoporous copper as versatile electrocatalysts for highly efficient water splitting. *Nat. Commun.* **2020**, *11*, 2940. [CrossRef] [PubMed]
10. Diao, J.; Qiu, Y.; Liu, S.; Wang, W.; Chen, K.; Li, H.; Yuan, W.; Qu, Y.; Guo, X. Interfacial Engineering of W2 N/WC Heterostructures Derived from Solid-State Synthesis: A Highly Efficient Trifunctional Electrocatalyst for ORR, OER, and HER. *Adv. Mater.* **2019**, *32*, e1905679. [CrossRef]
11. Jiang, C.; Wang, Y.; Zhang, Y.; Wang, H.; Chen, Q.; Wan, J. Robust Half-Metallic Magnetism in Two-Dimensional Fe/MoS2. *J. Phys. Chem. C* **2018**, *122*, 21617–21622. [CrossRef]
12. Shi, Y.; Zhou, Y.; Yang, D.-R.; Xu, W.-X.; Wang, C.; Wang, F.-B.; Xu, J.-J.; Xia, X.-H.; Chen, H.-Y. Energy Level Engineering of MoS2 by Transition-Metal Doping for Accelerating Hydrogen Evolution Reaction. *J. Am. Chem. Soc.* **2017**, *139*, 15479–15485. [CrossRef] [PubMed]
13. Stephenson, T.; Li, Z.; Olsen, B.; Mitlin, D. Lithium ion battery applications of molybdenum disulfide (MoS_2) nanocomposites. *Energy Environ. Sci.* **2014**, *7*, 209–231. [CrossRef]
14. Attanayake, N.H.; Thenuwara, A.C.; Patra, A.; Aulin, Y.V.; Tran, T.M.; Chakraborty, H.; Borguet, E.; Klein, M.L.; Perdew, J.P.; Strongin, D.R. Effect of Intercalated Metals on the Electrocatalytic Activity of 1T-MoS_2 for the Hydrogen Evolution Reaction. *ACS Energy Lett.* **2017**, *3*, 7–13. [CrossRef]
15. Liu, Q.; Li, X.; He, Q.; Khalil, A.; Liu, D.; Xiang, T.; Wu, X.; Song, L. Gram-Scale Aqueous Synthesis of Stable Few-Layered 1T-MoS2: Applications for Visible-Light-Driven Photocatalytic Hydrogen Evolution. *Small* **2015**, *11*, 5556–5564. [CrossRef] [PubMed]
16. Gan, X.; Lee, L.Y.S.; Wong, K.-y.; Lo, T.W.; Ho, K.H.; Lei, D.Y.; Zhao, H. 2H/1T Phase Transition of Multilayer MoS2 by Electrochemical Incorporation of S Vacancies. *ACS Appl. Energy Mater.* **2018**, *1*, 4754–4765. [CrossRef]
17. Xue, J.Y.; Li, F.L.; Zhao, Z.Y.; Li, C.; Ni, C.Y.; Gu, H.W.; Young, D.J.; Lang, J.P. In Situ Generation of Bifunctional Fe-Doped MoS2 Nanocanopies for Efficient Electrocatalytic Water Splitting. *Inorg. Chem.* **2019**, *58*, 11202–11209. [CrossRef] [PubMed]
18. Wan, K.; Luo, J.; Zhou, C.; Zhang, T.; Arbiol, J.; Lu, X.; Mao, B.W.; Zhang, X.; Fransaer, J. Hierarchical Porous Ni_3S_4 with Enriched High-Valence Ni Sites as a Robust Electrocatalyst for Efficient Oxygen Evolution Reaction. *Adv. Funct. Mater.* **2019**, *29*, 1900315. [CrossRef]
19. Yuan, F.; Wei, J.; Qin, G.; Ni, Y. Carbon cloth supported hierarchical core-shell NiCo2S4@CoNi-LDH nanoarrays as catalysts for efficient oxygen evolution reaction in alkaline solution. *J. Alloys Compd.* **2020**, *830*, 154658. [CrossRef]
20. An, L.; Feng, J.; Zhang, Y.; Wang, R.; Liu, H.; Wang, G.-C.; Cheng, F.; Xi, P. Epitaxial Heterogeneous Interfaces on N-NiMoO4/NiS2 Nanowires/Nanosheets to Boost Hydrogen and Oxygen Production for Overall Water Splitting. *Adv. Funct. Mater.* **2019**, *29*, 1805298. [CrossRef]
21. Li, B.; Li, Z.; Pang, Q.; Zhang, J.Z. Core/shell cable-like Ni_3S_2 nanowires/N-doped graphene-like carbon layers as composite electrocatalyst for overall electrocatalytic water splitting. *Chem. Eng. J.* **2020**, *401*, 126045. [CrossRef]
22. Yang, Y.; Zhang, K.; Lin, H.; Li, X.; Chan, H.C.; Yang, L.; Gao, Q. MoS2–Ni3S2 Heteronanorods as Efficient and Stable Bifunctional Electrocatalysts for Overall Water Splitting. *ACS Catal.* **2017**, *7*, 2357–2366. [CrossRef]
23. Zhang, J.; Wang, T.; Pohl, D.; Rellinghaus, B.; Dong, R.; Liu, S.; Zhuang, X.; Feng, X. Interface Engineering of MoS2/Ni3 S2 Heterostructures for Highly Enhanced Electrochemical Overall-Water-Splitting Activity. *Angew. Chem. Int. Ed. Engl.* **2016**, *55*, 6702–6707. [CrossRef] [PubMed]
24. Wu, X.; Zhang, T.; Wei, J.; Feng, P.; Yan, X.; Tang, Y. Facile synthesis of Co and Ce dual-doped Ni3S2 nanosheets on Ni foam for enhanced oxygen evolution reaction. *Nano Res.* **2020**, *13*, 2130–2135. [CrossRef]
25. Guo, Y.; Tang, J.; Henzie, J.; Jiang, B.; Xia, W.; Chen, T.; Bando, Y.; Kang, Y.M.; Hossain, M.S.A.; Sugahara, Y.; et al. Mesoporous Iron-doped MoS2/CoMo2S4 Heterostructures through Organic-Metal Cooperative Interactions on Spherical Micelles for Electrochemical Water Splitting. *ACS Nano* **2020**, *14*, 4141–4152. [CrossRef] [PubMed]
26. Zhou, G.; Li, M.; Li, Y.; Dong, H.; Sun, D.; Liu, X.; Xu, L.; Tian, Z.; Tang, Y. Regulating the Electronic Structure of CoP Nanosheets by O Incorporation for High-Efficiency Electrochemical Overall Water Splitting. *Adv. Funct. Mater.* **2019**, *30*, 1905252. [CrossRef]
27. Liu, G.; Thummavichai, K.; Lv, X.; Chen, W.; Lin, T.; Tan, S.; Zeng, M.; Chen, Y.; Wang, N.; Zhu, Y. Defect-Rich Heterogeneous MoS2/rGO/NiS Nanocomposite for Efficient pH-Universal Hydrogen Evolution. *Nanomaterials* **2021**, *11*, 662. [CrossRef]
28. Zhu, Q.L.; Xia, W.; Akita, T.; Zou, R.; Xu, Q. Metal-Organic Framework-Derived Honeycomb-Like Open Porous Nanostructures as Precious-Metal-Free Catalysts for Highly Efficient Oxygen Electroreduction. *Adv. Mater.* **2016**, *28*, 6391–6398. [CrossRef]

29. Wang, L.; Duan, X.; Liu, X.; Gu, J.; Si, R.; Qiu, Y.; Qiu, Y.; Shi, D.; Chen, F.; Sun, X.; et al. Atomically Dispersed Mo Supported on Metallic Co9S8 Nanoflakes as an Advanced Noble-Metal-Free Bifunctional Water Splitting Catalyst Working in Universal pH Conditions. *Adv. Energy Mater.* **2019**, *10*, 1903137. [CrossRef]
30. Li, B.; Zeng, H.C. Architecture and Preparation of Hollow Catalytic Devices. *Adv. Mater.* **2019**, *31*, e1801104. [CrossRef]
31. Xue, Z.; Liu, K.; Liu, Q.; Li, Y.; Li, M.; Su, C.-Y.; Ogiwara, N.; Kobayashi, H.; Kitagawa, H.; Liu, M.; et al. Missing-linker metal-organic frameworks for oxygen evolution reaction. *Nat. Commun.* **2019**, *10*, 5048. [CrossRef] [PubMed]
32. Thangasamy, P.; Oh, S.; Nam, S.; Randriamahazaka, H.; Oh, I.K. Ferrocene-Incorporated Cobalt Sulfide Nanoarchitecture for Superior Oxygen Evolution Reaction. *Small* **2020**, *16*, e2001665. [CrossRef] [PubMed]
33. Yan, J.; Kong, L.; Ji, Y.; White, J.; Li, Y.; Zhang, J.; An, P.; Liu, S.; Lee, S.-T.; Ma, T. Single atom tungsten doped ultrathin α-$Ni(OH)_2$ for enhanced electrocatalytic water oxidation. *Nat. Commun.* **2019**, *10*, 2149. [CrossRef]
34. Sha, L.; Liu, T.; Ye, K.; Zhu, K.; Yan, J.; Yin, J.; Wang, G.; Cao, D. A heterogeneous interface on NiS@Ni3S2/NiMoO4 heterostructures for efficient urea electrolysis. *J. Mater. Chem. A* **2020**, *8*, 18055–18063. [CrossRef]
35. Wang, D.; Zhang, X.; Shen, Y.; Wu, Z. Ni-doped MoS2 nanoparticles as highly active hydrogen evolution electrocatalysts. *RSC Adv.* **2016**, *6*, 16656–16661. [CrossRef]